

Microstructure Evolution and Mechanical Properties of Ti–6Al–4Zr–4Nb Alloys Fabricated by Spark Plasma Sintering (SPS)



S.J. LIANG, S. MATSUNAGA, Y. TODA, T. MATSUNAGA,
and Y. YAMABE-MITARAI

The near- α Ti–6Al–4Zr–4Nb (wt pct) alloy is a recently developed alloy with potential for aerospace applications. This study evaluates the microstructure and mechanical properties of Ti–6Al–4Zr–4Nb produced by spark plasma sintering (SPS). The SPS samples sintered in the $\alpha + \beta$ regions exhibited equiaxed α with a neighboring thin β phase. Above the β -transus temperature, the α/β lamellar structure formed, allowing control of the grain size (100 ~ 200 μm). The compressive strength and the creep property of the SPS samples were compared with the LPBFed and the forged samples. The compressive strength of the SPS sample was lower than that of the LPBFed sample but similar to the forged sample. The SPS samples exhibited longer creep rupture life (2220 hours) than LPBFed samples (1730 hours), but shorter than the forged sample (4109 hours). The creep deformation mechanism of the lamellar structure in the SPS sample was dislocation creep.

<https://doi.org/10.1007/s11661-024-07422-8>
© The Author(s) 2024

I. INTRODUCTION

IN recent years, as the air transportation industry has played an increasingly important role in global economic activities, the demand for aircraft is also increasing.^[1] The near- α titanium alloy is exclusively used in jet engine compressor blades and other components due to its excellent high-temperature strength, high-temperature creep properties, and fatigue properties. The near- α titanium alloys primarily exhibit the α -phase and a small amount of the high formability β -phase.^[2] At present, commercial high-temperature near- α titanium alloys are produced by forging and/or rolling process. They mainly show the bi-modal structure, which consists of a mixture of equiaxed α -phase and $\alpha + \beta$ lamellar structures.^[3] Mishra *et al.* reported that eliminating the equiaxed α -phase in a bi-modal structure can substantially improve the high-temperature creep rupture life of the

material.^[4] To balance creep and fatigue properties, the grain size needs to be around 100 μm or less.^[5] To obtain such a small grain size, performing thermomechanical processing in the $\alpha + \beta$ phase region is necessary; however, eliminating equiaxed α -phase is difficult by thermal processing in the $\alpha + \beta$ phase region. This motivates us to seek a new manufacturing process to fabricate the lamellar structure while preventing equiaxed α phase formation.

Furthermore, conventional fabrication methods usually produce a lot of material waste due to machining the part with complex geometries.^[6] In order to improve energy and cost efficiency, additive manufacturing techniques such as laser power bed fusion (LPBF) and electron beam melting (EBM) have been recently introduced as attractive new manufacturing processes.^[7–9] In these processes, the metal powders are melted and rapidly solidified by laser or electron beam, which minimizes the machining process, thereby reducing the materials waste and allowing us to have much more complex designs and shapes.^[9] Previously, Kuroda and Yamabe-Mitarai *et al.*^[10,11] investigated the microstructure and high-temperature mechanical properties of Ti–6Al–4Zr–4Nb fabricated by LPBF. The melting pool boundaries formed during the LPBF process and they remained during heat treatment. Inside the melt pool boundaries, the martensite structure is formed by the rapid cooling rate of LPBF. The martensite structure changed to the lamellar structure and the equiaxed- α phase also formed along the melting pool boundaries

S.J. LIANG, S. MATSUNAGA, and Y. YAMABE-MITARAI are with the Department of Advanced Materials Science, Graduate School of Frontier Sciences, The University of Tokyo, 5-1-5 Kashiwanoha, Kashiwa, Chiba 277-8561, Japan. Contact e-mail: mitarai.yoko@edu.k.u-tokyo.ac.jp Y. TODA is with the National Institute for Materials Science, 1-2-1 Sengen, Tsukuba, Ibaraki 305-0047, Japan. T. MATSUNAGA is with the Institute of Space and Astronautical Science, Japan Aerospace Exploration Agency, 3-1-1 Yoshinodai, Chuo-ku, Sagami-hara, Kanagawa 252-5210, Japan.

Manuscript submitted November 26, 2023; accepted April 22, 2024.

during heat treatment. In other LPBF conditions with a slow cooling rate, the lamellar microstructure without the equiaxed- α phase formed. It was found that the equiaxed- α phase along the melting pool boundaries and minor defect formation during LPBF ultimately cause the decrease of creep rupture life. Therefore, we have explored to find a more suitable manufacturing method.

Spark plasma sintering (SPS) is the powder process that allows fast sintering and producing denser samples without defect.^[12] SPS allows for quick homogenization of the alloy during the sintering process by accelerating the diffusion of solute atoms compared to other processes such as hot pressing (HP). This indicates that SPS has an excellent performance in preparing a homogeneous microstructure in final products.^[13] The SPS method possesses a great advantage in improving the microstructure and material densities. SPS has been applied for some near- α titanium alloys,^[14] but in most cases, it has been applied for dispersion-strengthened titanium alloys that the alloy matrix is strengthened by intermetallic compounds, carbides, oxides, borides, and nitrides.^[14,15] This is because the distribution of these particles can be controlled well in the SPS process compared with the casting and hot deformation process.

Therefore, in this study, the SPS was utilized to fabricate near- α titanium alloys to form the homogeneous lamellar microstructure by controlling the sintering temperature. The microstructure and mechanical properties of SPS samples were evaluated and compared to samples fabricated by forging or LPBF to clarify the correlation between processing, microstructure, and mechanical properties. Investigating the processing-structure-property relationships allows us to explore and suggest the appropriate application scenarios.

II. EXPERIMENTAL

A. Selection of Target Material

Ti-6Al-4Zr-4Nb was selected as a target alloy. Most of the commercially available high-temperature titanium alloys, such as TIMETAL834^[16] and Ti-1100,^[17] contain Sn as an additional element. While Sn is excellent in solid solution strengtheners, it also deteriorates oxidation resistance.^[18,19] Ti-6Al-4Zr-4Nb was designed to improve oxidation resistance.^[19-23] Based on Ti-6Al, Nb was added to increase oxidation resistance, and Zr was added for solid solution strengthening, while Sn was excluded.^[22]

B. Preparation of Ti-6Al-4Zr-4Nb Alloys by SPS

The alloy powder of Ti-6Al-4Zr-4Nb prepared by TANIOWIS GmbH was used as the starting material. The particle size was distributed between 16 and 52 μm and the average particle size was 30 μm . Figure 1 shows the SEM image of the powders, and Table I shows the nominal composition.

The β transus temperature of Ti-6Al-4Zr-4Nb is between 900 and 1000 $^{\circ}\text{C}$.^[19] To fabricate the samples

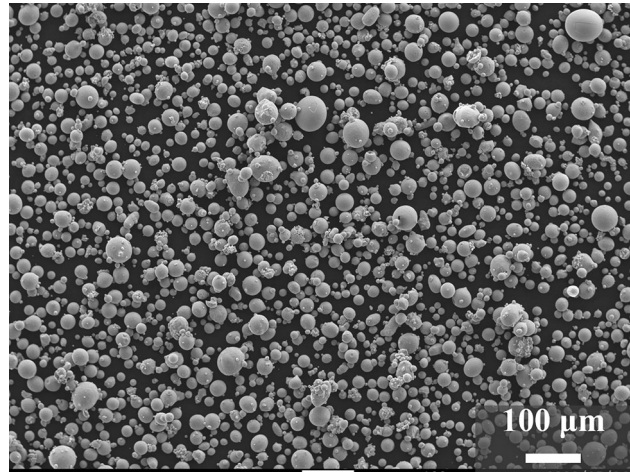


Fig. 1—SEM-secondary electron image of Ti-6Al-4Zr-4Nb powder.

(SPS-1 to SPS-5), the Ti-6Al-4Zr-4Nb powders were directly put into in cylindrical graphite die with a dimension of 10 mm in diameter and 10 mm in height without pre-pressing. The sintering condition was selected to observe microstructure change at 800 $^{\circ}\text{C}$, 900 $^{\circ}\text{C}$, 950 $^{\circ}\text{C}$, 1100 $^{\circ}\text{C}$, and 1200 $^{\circ}\text{C}$ for 5 minutes in an Ar atmosphere under a pressure of 90 MPa using our in-house SPS equipment (SPS-515S, DR. SINTER LAB). The temperature was measured by a pyrometer during the SPS sintering. The sintering conditions are shown in Table II. Furthermore, to evaluate the mechanical properties, a larger disk-shaped sample of 52 mm in diameter and 15 mm in height was sintered at 1100 $^{\circ}\text{C}$ for 10 minutes in an Ar atmosphere under a pressure of 30 MPa, prepared by NJS Co., Ltd SPS Center, Japan, shown as SPS-6 in Table II. The preparation conditions for the forged and LPBF samples with the same alloy composition, which were used as comparison materials, are shown in the previous works.^[10,19]

C. Microstructure Characterization

All samples were cut in a direction parallel to the sintering axis and observed using scanning electron microscopy (FE-SEM, JSM-7200F, JEOL) at an accelerating voltage of 20 kV to investigate the differences in microstructure due to differences in fabrication temperatures and fabrication methods. In addition, the phase composition analysis was performed for each phase using an energy-dispersive X-ray spectrometer (EDS, JSM-7200F, JEOL) at an accelerating voltage of 20 kV. The crystal orientation and average grain size were analyzed by electron backscatter diffraction (EBSD) JSM-7200F JEOL at an acceleration voltage of 20 kV. The phase volume fraction was calculated by ImageJ using backscattered electron images.

D. Mechanical Tests

SPS-6 was used for mechanical tests. Figure 2 illustrates the preparation of mechanical test specimens cut

from the SPS-6 sample. The compression test specimens with $3 \times 3 \times 5.5$ mm in size were extracted parallel to the sintering axis. Creep test specimens with a diameter of 3 mm and a gauge length of 13.5 mm were cut perpendicular to the sintering axis. Using rectangular solid specimens, the compression tests were performed at room temperature, 300, 400, 500, and 600 °C at a strain rate of 3.0×10^{-4} /s in a vacuum using a Shimadzu AG-X high-temperature universal testing machine. The creep test was conducted at temperatures of 550 °C and 600 °C under a constant stress of 139 MPa until rupture. In order to investigate the high-temperature creep deformation mechanism, multi-step creep tests were conducted by varying the stresses of 69, 104, 139, 174, 208, 243, and 278 MPa, with temperatures of 550 °C and 600 °C, respectively.

III. RESULTS AND DISCUSSION

A. Phase Composition and Microstructure

The backscattered electron images of samples (SPS-1 to 5) are shown in Figure 3. When the sintering temperature was in the α phase region, a single equiaxed α -phase was observed in the SPS-1 as shown in Figure 3(a). Some micropores were also observed as marked in red allows and rectangles, indicating the sintering process did not finish perfectly due to the low sintering temperature.^[24] After sintering in the $\alpha + \beta$ phase region at 900 and 950 °C, an equiaxed α -phase (dark phase) with an average grain size of about 12 μ m and a thin β -phase (bright phase) were identified as shown in Figures 3(b) and (c), according to the previous study.^[10] When the sintering temperature was in the β -phase region at 1100 and 1200 °C (Figures 3 (d) and (e)), both obtained the $\alpha + \beta$ lamellar structure with an average grain size (prior β -grain) of 100 μ m analyzed by electron backscatter diffraction (EBSD). These structures align with the reports on other near- α alloys synthesized in the β -phase region using the SPS

Table I. Nominal Chemical Composition of Ti-6Al-4Zr-4Nb Powder in Weight Percent (Wt Pct)

Ti	Al	Zr	Nb	Fe	C	O	N	H
Bal.	6	4	4	0.01	0.01	0.3	0.01	0.03

method.^[14,25,26] The microstructures of SPS-6 for the mechanical test are also shown in Figure 4 together with SPS-4, both sintered at 1100 °C. As shown in Figure 4, the $\alpha + \beta$ lamellar structure was observed in both SPS-6 and SPS-4, but the average grain size of SPS-6 was 200 μ m analyzed by the reconstructed image of the β phase from α phase using electron backscatter diffraction (EBSD), while it is 100 μ m in SPS-4 as shown in Figures 4(a) and (c). The interlamellar spacing of SPS-6 was 7 ± 1 μ m (Figure 4(b)), while it was 1.5 ± 0.5 μ m in SPS-4 (Figure 4(d)). The large difference in the interlamellar spacing is due to the size of the samples. The specimen size of SPS-6 is 52 mm in diameter and 15 mm in height, larger than that of SPS-4, with 10 mm in diameter and 10 mm in height. This is because the cooling rate of SPS-6 is slower than that of SPS-4 as shown in Table II. A slow cooling rate caused the formation of a coarse lamellar structure.

To reconfirm that the phases present in the lamellar structure are the α - and β -phases, respectively, the SPS-6

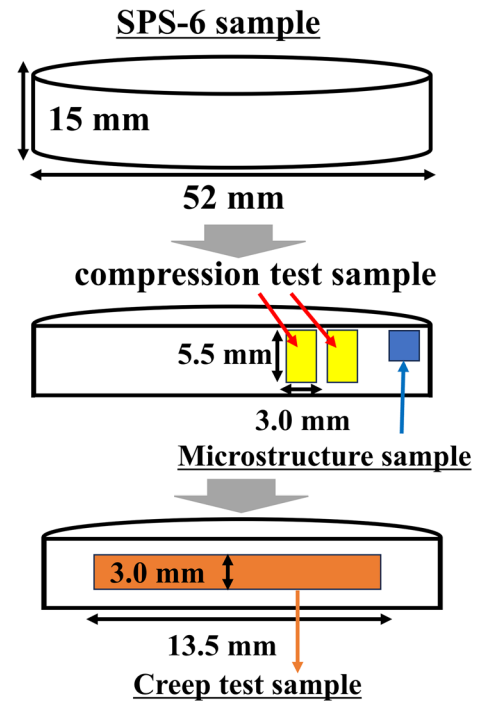


Fig. 2—The preparation of mechanical test specimens cut from the SPS-6 sample.

Table II. Sintering Conditions of SPS Samples

Sample No.	Sintering Temperature (°C)	Phase Region	Pressure (MPa)	Heating Rate (°C/min)	Holding Time (min)	Cooling Rate (°C/min)
SPS-1	800	α	90	60	5	45
SPS-2	900	$\alpha + \beta$				
SPS-3	950					
SPS-4	1100	β				
SPS-5	1200					
SPS-6	1100		30	25	10	18

SPS-1 to SPS-5 were fabricated by in-house SPS machine, whereas larger SPS-6 was fabricated by NJS Co., Ltd SPS Center, Japan.

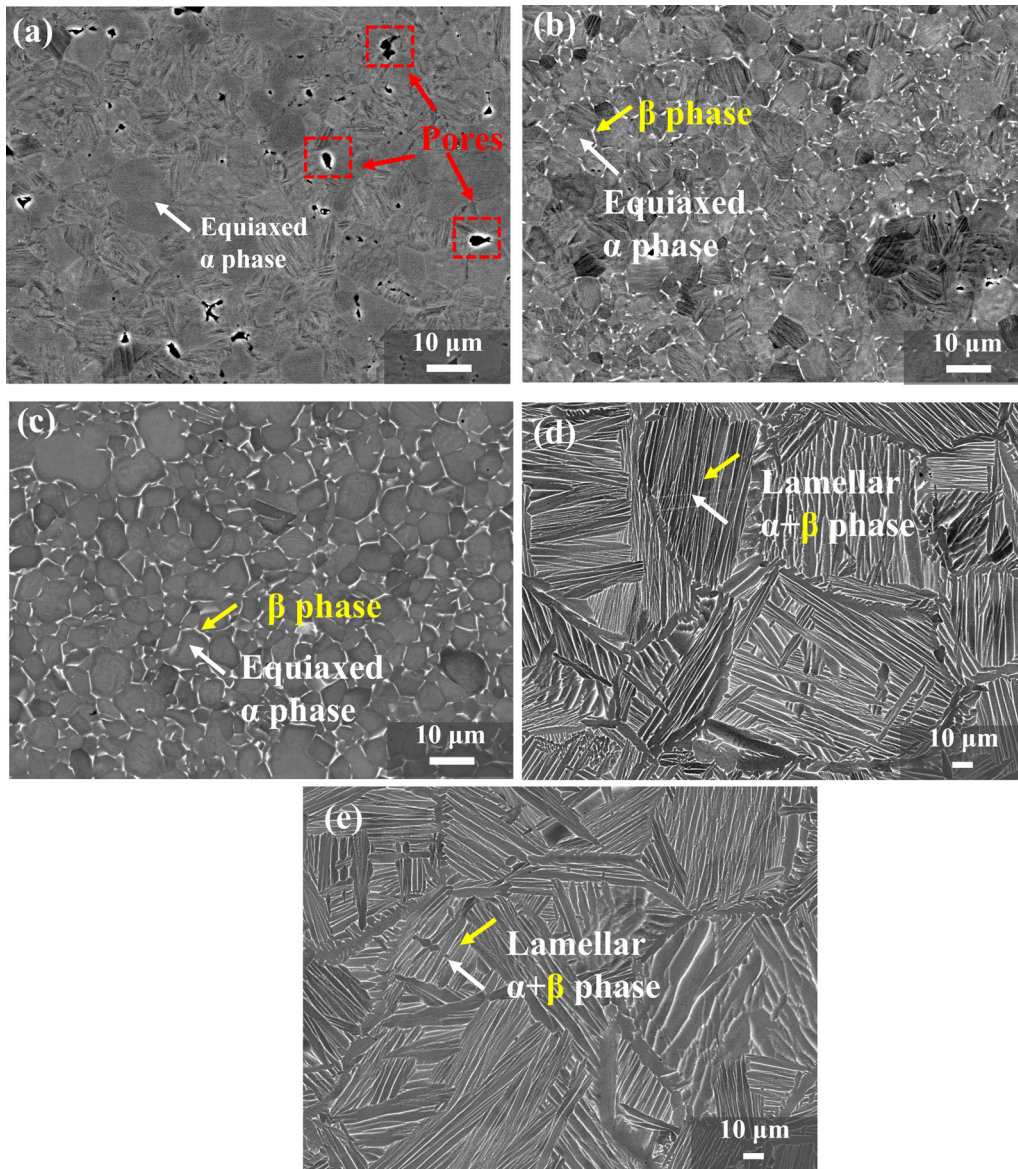


Fig. 3—Back-scattered electron images of Ti-6Al-4Zr-4Nb fabricated by SPS with different sintered conditions: (a) SPS-1, 800 °C, (b) SPS-2, 900 °C, (c) SPS-3, 950 °C, (d) SPS-4, 1100 °C, (e) SPS-5, 1200 °C.

specimen was chosen and analyzed using energy-dispersive spectroscopy (EDS) and electron backscatter diffraction (EBSD). The EDS mappings and EBSD phase map are presented in Figure 5. The dark phase was identified as α -phase, whereas the thin bright phase was identified as β -phase as shown in Figure 5(b). While the α -phase exhibited high Al content, the β -phase exhibited high Zr and Nb content as shown in Figure 5(g).

B. Comparison of Microstructures Among SPS, forged, LPBF Samples

The microstructure of SPS samples is compared with the ones of the forged and LPBFed samples with the same composition of Ti-6Al-4Zr-4Nb.^[10,11,19] Table III summarizes the differences in microstructures obtained

by SPS, forging, and LPBF. Forged-1 and Forged-2 were forged and rolled at 900 °C and heat treated at 950 °C in the $\alpha + \beta$ phase region (Forged-1) and 1000 °C in the β -phase region (Forged-2).^[19] At the $\alpha + \beta$ phase region (950 °C), Forged-1 showed a bi-modal microstructure, while the SPS-3 sample exhibited equiaxed α and β microstructures. Generally, when Ti alloys with the α and β two phases are cooled by a fast-cooling rate, the equiaxed α phase remains while the β phase transforms to α phase with Burgers relationship, thereby the lamellar structure is formed (bi-modal structure).^[5] In this case, the composition of the α phase is not equilibrium due to a lack of diffusion time. When Ti alloys with two phases are cooled slowly, the β phase gradually transformed to α phase with sufficient diffusion, and then the thin β phase remains around the equiaxed α grains. In this case, the compositions of the α

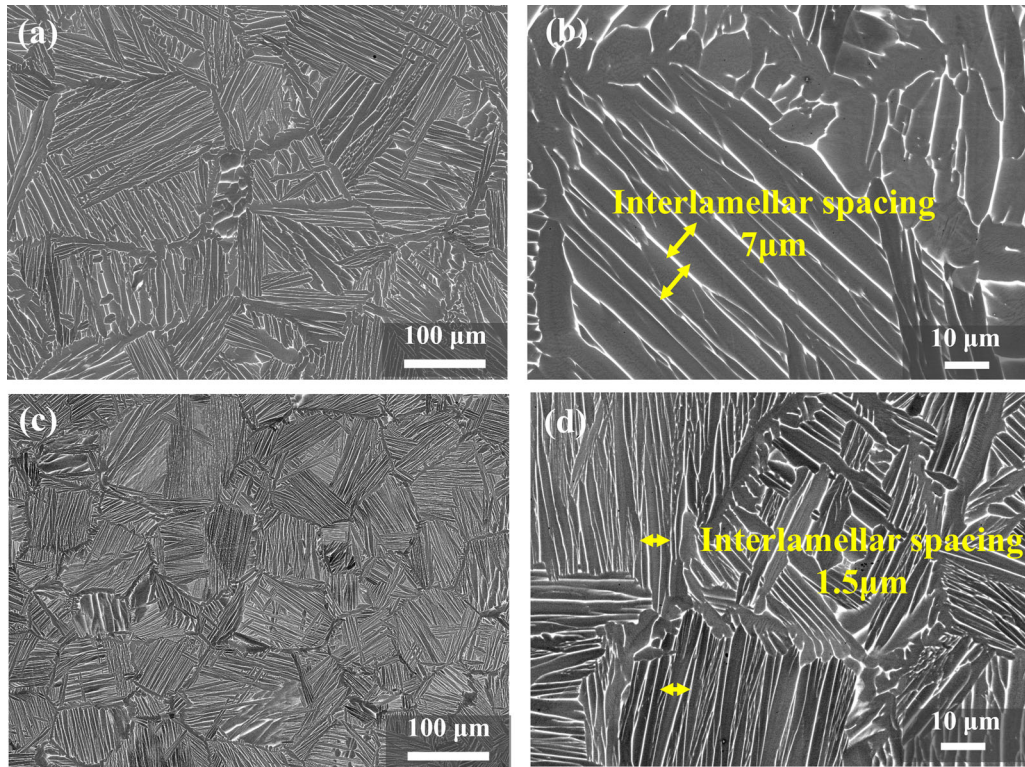


Fig. 4—Back-scattered electron images of (a, b) SPS-6 and (c, d) SPS-4.

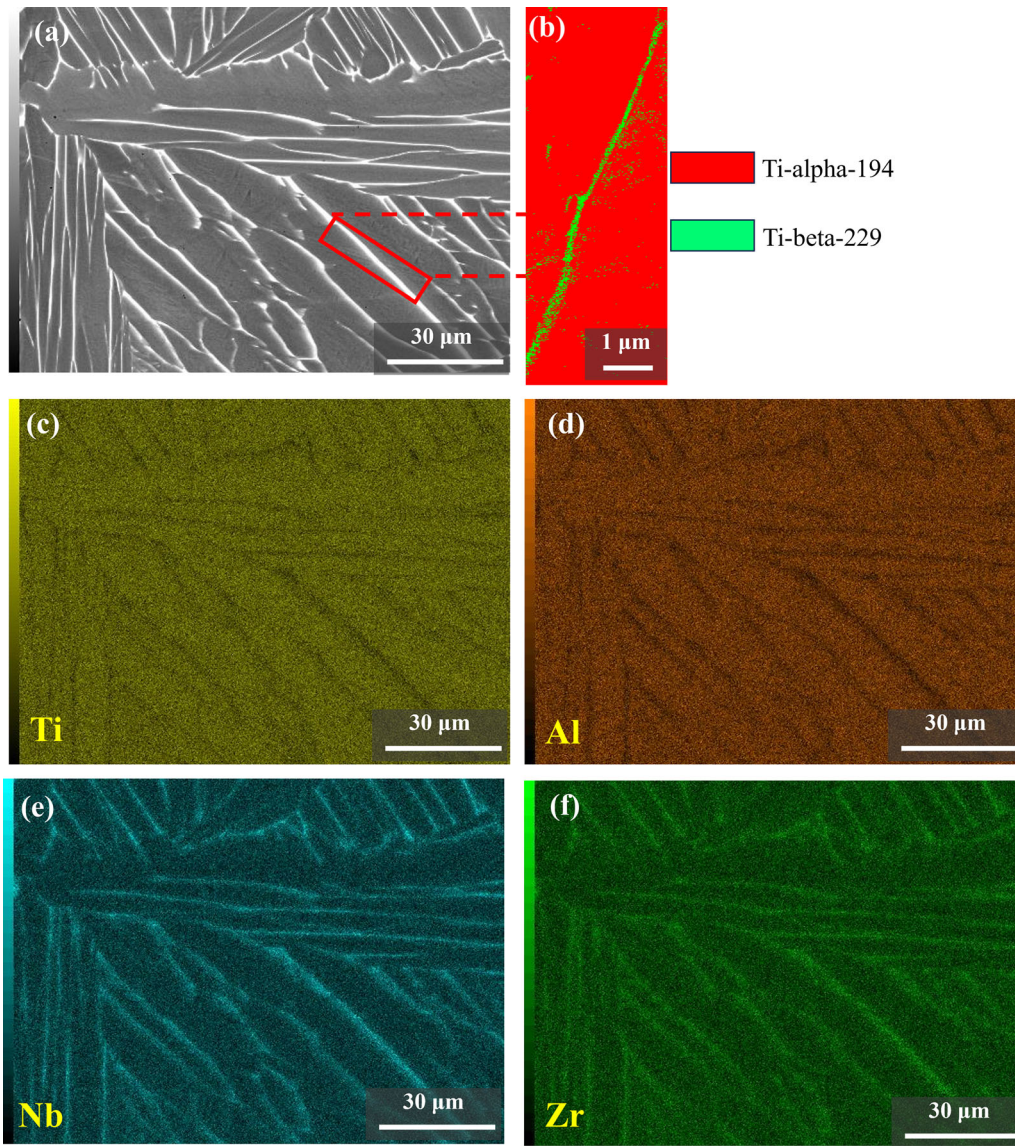
phase are close to equilibrium due to enough diffusion time. The equiaxed α grains in SPS samples indicate a slower cooling rate (45 °C/min) than the forged samples (600 °C/min). Similarly, in previous SPS studies focusing on the typical near- α alloy Ti64 and CP-Ti, the microstructure characterized by a dominant α phase surrounded by a β phase was reported when specimens were sintered in the $\alpha + \beta$ phase region.^[25,27–29] This consistency in microstructural morphology across different studies underscores the difficulty of bi-modal structure formation only by the SPS method.

Three different LBPf processing conditions were also compared to SPS-6 samples sintered in the β -phase region as shown in Table III. Heat treatment was also applied after LBPf processing.^[10,11] The LBPf-A and -B samples showed a martensite structure in the as-build sample due to a faster cooling rate, while $\alpha + \beta$ lamellar structure was formed in the as-build LBPf-D sample with a relatively slower cooling rate.^[10] The melting pool boundaries with approximately 100 μm were observed in both LBPf-A and B samples while melting pool boundaries were eliminated and grain growth occurred in the LBPf-D sample. The grain size of the LBPf-D sample was approximately 300 μm . After heat treatment at the $\alpha + \beta$ phase region (950 °C), the martensite structure transformed into a mixture of the remaining equiaxed α -phase and lamellar structure in the LBPf-B sample. In the case of heat treatment in the β -phase region, the lamellar structure formed, but no equiaxed α phase formed in the LBPf-A sample.

Regardless of the processing methods, a lamellar structure formed by heat treatment in the β -phase region

(1100 °C) in the Forged-2, LBPf-A, and SPS-6 samples because α phase once soluted in the β phase during heat treatment and the plate-like α phase reformed in β phase during cooling.^[10,11,19] The grains of the Forged-2 sample grew fast and the grain size was measured at 500 μm , which exceeded that of the SPS-6 sample (200 μm), LBPf-A (100 μm), and LBPf-D (300 μm). On the other hand, in the LBPf-A sample, the melting pool boundaries were not eliminated in the β phase region, and the melting pool width was maintained at approximately 100 μm .^[11] Compared to the forged and LBPf samples, the SPS process enables grain size control through the manipulation of time, temperature, and pressure, as demonstrated in Figure 4 and other reports.^[30]

The SPS-6 sample exhibited a larger interlamellar spacing (7 μm) compared to the Forged-2 sample (2 μm), LBPf-A sample (1 μm), and LBPf-D sample (3 μm). Significant differences were also observed in the morphology of the β -phase within the $\alpha + \beta$ lamellar structure among the Forged-2, SPS-6, and LBPf-D samples. Specifically, the Forged-2 and SPS-6 samples displayed a thinner and linear morphology of the β -phase, while the LBPf-D samples exhibited a thicker and bulkier rod-like morphology. The volume fraction of α and β phase of the lamellar microstructure with magnification ($\times 500$) for the SPS-6 sample was measured by ImageJ software and summarized in Table IV, while the Forged-2 and LBPf-D samples with the same magnification ($\times 500$) were also added for comparison. This result indicates a higher volume fraction of the β -phase in the LBPf-D samples compared to the SPS-6



(g) Element (wt%)	Ti	Al	Zr	Nb	Volume Fraction (%)
Dark region (α -phase)	88.8	5.6	3.2	2.4	85.4
Bright region (β -phase)	88.7	3.6	2.9	4.8	14.6

Fig. 5—SEM-EBSD and EDS analysis of the lamellar microstructure in SPS-6 sample: (a) Back-scattered electron image, (b) Phase map by EBSD analysis, (c–f) Distribution of constituent elements by EDS analysis, (g) Average compositions and volume fraction of the α and β phase in the lamellar microstructure (a) of the SPS-6 sample.

and Forged-2 samples. This comparison also underscores significant differences in phase distribution between the different processing methods.

Based on these findings, it can be inferred that the SPS process offers distinct advantages over forging and LPBF in terms of simplicity and rapid prototyping for fabricating $\alpha + \beta$ alloys with a uniform equiaxed or

Table III. The Characteristics of the Microstructures Obtained Through SPS, Forge, and LPBF Manufacture Process at $\alpha + \beta$ and β Temperature Regions

Manufacturing Process	Condition of Process	Cooling rate (°C/min)	Constituent Phases	Grain size (μm)	Interlamellar Space (μm)
SPS-3	950°C, 90MPa FC	45	Equiaxed- α phase + low volume fraction of β -phase	12	-
SPS-6	1100 °C, 30MPa FC	18	Lamellar	200	7
Forged-1 ^[19]	900 °C HT: 950 °C, 3 hours AC	600	Bi-modal	10	-
Forged-2 ^[19]	900 °C HT: 1000 °C, 3 hours AC	600	Lamellar	500	2
LPBF-B ^[10]	Laser power: 300 W Scan speed: 1200mms ⁻¹ HT: 650 °C 3 hours + 950 °C 2 hours WQ		Lamellar Equiaxed- α	100	1
LPBF-D ^[10]	Laser power: 360 W Scan speed: 1200mms ⁻¹ HT: 650 °C 3 hours + 950 °C 2 hours WQ		Lamellar	300	3
LPBF-A ^[11]	Laser power: 300 W Scan speed: 1000mms ⁻¹ HT: 1100 °C 2 hours AC		Lamellar	100	3

HT heat treatment, *FC* furnace cooling, *AC* air cooling, *WQ* water quench

Table IV. The Volume Fraction of α and β Phase for SPS-6, Forged-2, and LPBF-D Samples

Sample	SPS-6	LPBF-D	Forged-2
Volume Fraction of α Phase (Pct)	86.1	82.0	90.9
Volume Fraction of β Phase (Pct)	13.9	18.0	9.1

lamellar structure. The SPS process allows for precise control over grain size, promoting enhanced microstructural uniformity. However, in scaling up it is important to consider the effects of thermal gradient in achieving a uniform microstructure. Furthermore, the absence of the columnar and melt pool solidification structure in the SPS samples suggests the potential of SPS in mitigating certain microstructural defects associated with other manufacturing processes. These insights highlight the academic and practical significance of the SPS technique in advancing the fabrication of near- α alloys.

C. Mechanical Properties

1. High-temperature compression test

The mechanical properties of the SPS-6 sample with a lamellar microstructure and a grain size of 200 μm were systematically investigated through compression and creep tests.

The 0.2 pct proof stress of the compression test from RT to 600 °C is summarized in Table V. The compression strengths of the Forged-2, LPBF-B, D, and SPS-6 with lamellar microstructure are compared in Figure 6.^[10,19] The microstructures of the compared

Table V. The 0.2 pct Proof Stress of SPS-6 Samples Obtained by Compression Test

Test temperature (°C)	RT	300	400	500	600
0.2 pct proof stress (MPa)	999	556	488	451	433

samples are all lamellar structures. Then, compared by grain size, it is known that strength is proportional to $-1/2$ power of grain size according to the well-known Hall-Petch relationship. The strength of the sample with a smaller grain size is higher than that of the samples with a larger grain size. However, Figure 5 indicates the strength is not governed by grain size. The interlamellar spacing also governs the strength because the interface between α and β interrupts dislocation movement. The smaller interlamellar spacing increases the strength. However, the strength is not explained by interlamellar spacing since the interlamellar spacing of the LPBF-B, D, and the forged samples is almost the same, 1 ~ 3 μm , while that of the SPS-6 is 7 μm .

Compared with LPBF-B and the Forged-2 with similar interlamellar spacing, the strength of the LPBF-B was higher than that of the Forged-2. This is

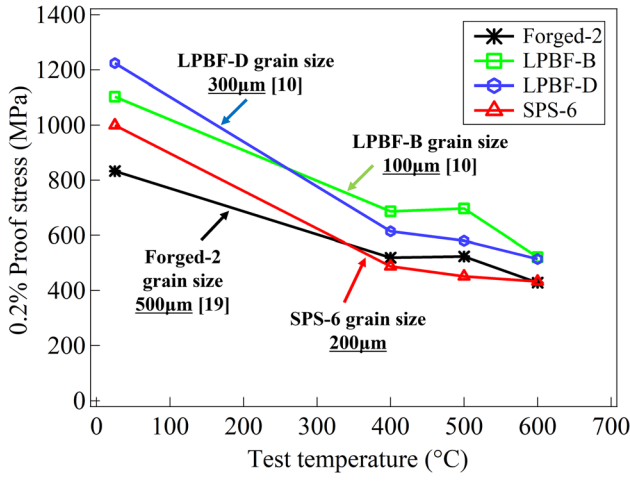


Fig. 6—Comparison of the 0.2 pct proof stress in RT, 300, 400, 500, and 600 °C of samples prepared by forging, LPBF, and SPS.

due to the small grain size in the LPBF-B. Compared with LPBF-D and SPS-6 with similar grain size, the strength of the LPBF-D was higher than that of the SPS-6. This is due to smaller interlamellar spacing in LPBF-D than in SPS-6. Overall, the combination of grain size and interlamellar spacing determines the order of the strength among the tested alloys.

2. Tensile creep test

The creep test was performed for the SPS-6 sample at a test temperature of 600 °C under the applied stress of 139 MPa. The creep curve is shown by the red line in Figure 7 together with the creep curves of the Forged-1, 2,,^[19] LPBF-A, B, and D.^[10,11] The creep curves of HIPed LPBF-B and -D samples^[10] are also shown in Figure 7. The SPS-6 sample exhibited a rupture life of 2220 hours, which was the second longest of all samples tested, after the Forged-2 sample. The creep life of the SPS-6 sample was longer than LBPf samples. The LBPf samples improved creep life by hot isostatic pressing (HIP) due to the elimination of micropores introduced during processing.^[10]

3. Analysis of creep deformation mechanisms of the Ti-6Al-4Zr-4Nb alloys fabricated by SPS

The creep curves for the multi-step creep test are shown in Figure 8. At both temperatures, the strain rate remained small up to 174 MPa, but it increased drastically above 174 MPa.

Through the analysis of the step creep test results, the stress exponent n can be determined, which provides valuable insights into the predominant deformation mechanism, such as diffusion creep or dislocation creep.^[31] At high temperatures, the deformation of the material exhibits power-law creep characteristics. In power-law creep, the strain rate $\dot{\epsilon}$ can be mathematically expressed by the following equation.^[32]

$$\dot{\epsilon} = A_0 \frac{G\Omega D}{k_b T b^2} \left(\frac{b}{d_g}\right)^p \left(\frac{\sigma}{G}\right)^n \quad [1]$$

where A_0 , G , Ω , k_b , T , σ , b , d_g , n , p , and D is constant,

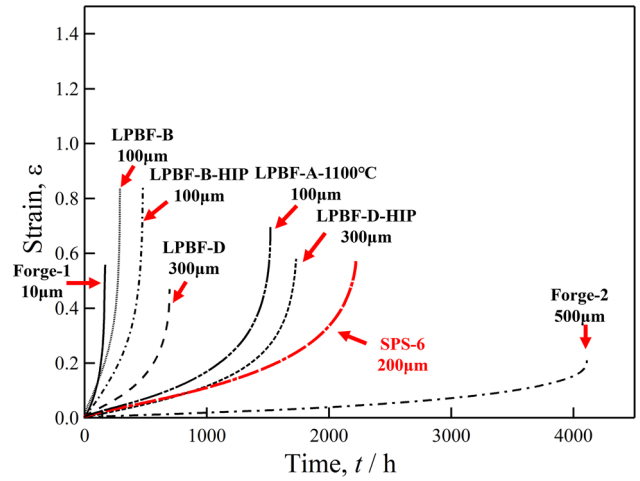


Fig. 7—Creep rupture life of samples of Forged-1, Forged-2, SPS-6, LPBF-A, LPBF-B, LPBF-B with HIP, LPBF-D, and LPBF-D with HIP at 600 °C, 139 MPa.

shear modulus, volume of the atom, Boltzmann's constant, absolute temperature, applied stress, Burgers vector, grain size, stress exponent, grain size exponent, and the effective diffusion coefficient, respectively. Since the experimental conditions remain unchanged, the various parameters in the equation can be considered as constants A , and then Eq. [1] can be transformed into the following Eq. [2].

$$\dot{\epsilon} = A\sigma^n \quad [2]$$

By considering A as a constant, taking the logarithm of both sides of the equation simultaneously [3], and performing mathematical manipulation, the equation for the stress exponent n can be derived [4]. This equation reveals that the value of n can be determined by plotting the double logarithmic plot between the stress and the strain rate, providing the dominant deformation mechanism.^[33]

$$\ln \dot{\epsilon} = n \ln \sigma \quad [3]$$

$$n = \frac{\ln \dot{\epsilon}}{\ln \sigma} \quad [4]$$

Therefore, based on the creep curve shown in Figure 8, the steady-state creep strain rate was calculated. Subsequently, a double logarithmic plot of the steady-state creep strain rate and the applied stress was drawn as depicted in Figure 9. The obtained stress exponents n are shown in Table VI. At 550 °C, the stress exponent, n , was determined to be 5.5. The datum at 69 MPa is not on a linear relationship. At 600 °C, the stress exponent, n , was determined as 0.5 with lower applied stresses ($\sigma \leq 174$ MPa), while it demonstrated a substantial increase to 4.0 with higher applied stresses ($\sigma \geq 174$ MPa).

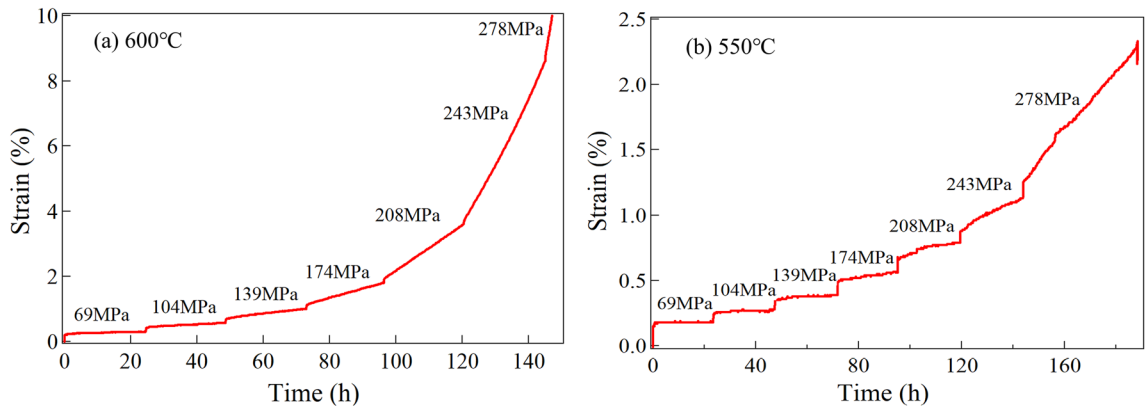


Fig. 8—Creep curves for the step creep test at (a) 600 °C, (b) 550 °C.

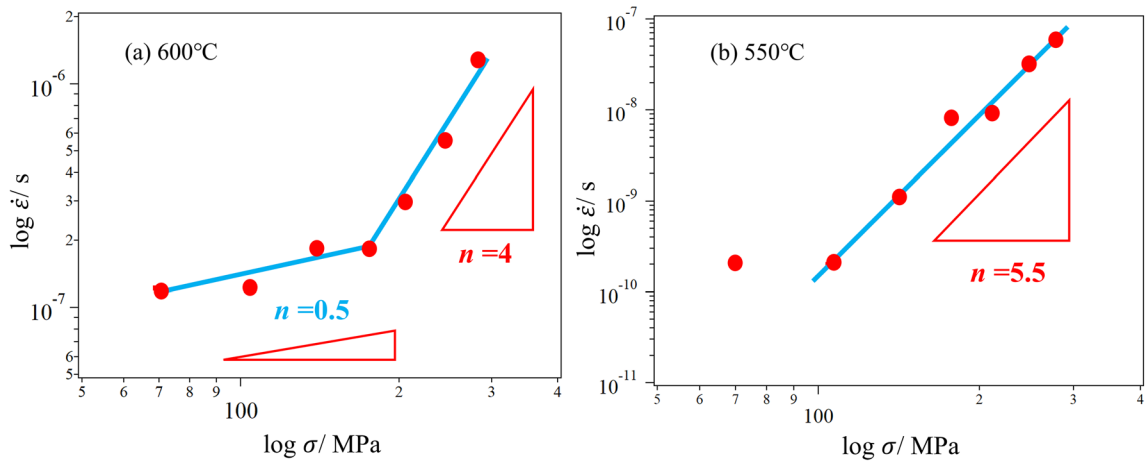


Fig. 9—The steady-state creep strain rate as a function of the applied stresses at (a) 600 °C, (b) 550 °C.

4. Creep deformation mechanisms of the Ti-6Al-4Zr-4Nb alloys fabricated by SPS

In steady-state creep, there are three primary deformation mechanisms: (1) dislocation creep dominated by the movement of dislocations, (2) grain boundary sliding dominated by the movement of grain boundaries, and (3) diffusion creep which contains grain boundary diffusion (coble) and lattice diffusion (Nabarro-herring).^[34] Each mechanism is associated with a specific range of stress exponents. When the stress exponent reaches 2, grain boundary sliding becomes the dominant mechanism, whereas stress exponents in the range of 3-8 indicate dislocation creep governed by dislocation motion.^[35] The SPS-6 sample exhibits a stress exponent of 4 to 5, indicating that the dominant deformation mechanism is dislocation creep. In addition, a low-stress exponent, 0.5, was observed at low applied stress at 600 °C. The low-stress exponent of about 1 indicates diffusion creep.^[34] However, the deformation map indicates a strain rate of 10^{-7} /s and grain size of 200 nm located in the high-temperature dislocation creep.^[19] So, further investigation is necessary for low-stress levels at 600 °C.

The dominant creep deformation mechanism of the LPBF samples in Ti-6Al-4Zr-4Nb was grain boundary sliding at low applied stress ($\sigma \leq 150$ MPa), while it shifted to dislocation creep at high applied stress ($\sigma \geq 150$ MPa) at 600 °C.^[11] In the LPBF-B sample, the equiaxed α phase with a diameter of 10 μ m formed along melting boundaries, whereas there was no equiaxed α phase in the LPBF-A sample.^[11] The presence of the equiaxed α phase accelerates grain boundary sliding, resulting in a shorter creep life for the LPBF-B compared to that of LPBF-A.

In the forged samples, the dominant creep deformation for the equiaxed α phase structure, the bi-modal structure, and the lamellar structure was dislocation creep at 550 °C under high applied stress, while grain boundary sliding became dominant at the low applied stress.^[36] These results indicate creep deformation mechanism is independent of the process and microstructure. In the temperature range between 550 and 600 °C, the creep deformation mechanism transitions from grain boundary sliding at lower applied stress ($\sigma \leq 150$ MPa) to dislocation creep at high applied stress ($\sigma \geq 150$ MPa). The grain boundary sliding becomes dominant in the samples with smaller grains

Table VI. Stress Exponent, n of the Steady-State Creep Strain Rate of SPS-6 Sample

Test Temperature	600 °C		550 °C
Stress Range (MPa)	$\sigma \leq 174$	$\sigma \geq 174$	$\sigma \geq 139$
n	0.5	4.0	5.5

than 100 μm . This behavior is consistent with the findings in forged commercial Ti alloys, where dislocation creep was dominant between 400 and 600 °C.^[33,37-41] LPBF samples of commercial Ti-6Al-4V with a martensite structure were predominantly deformed by dislocation creep between 450 and 650 °C.^[42,43] These results further support the notion that the deformation mechanism of Ti alloys is independent of alloy composition, process, and microstructure.

5. Creep rupture life

Creep rupture life varied even with the same deformation mechanism, as depicted in Figure 7. For instance when comparing SPS-6 and LPBF-D with similar grain size, the creep rupture life of the SPS-6 sample was longer than that of LPBF-D, despite their similar creep strain rates up to 1000 hours. Anisotropy of diffusion and microstructure also plays a role in affecting creep rupture life.^[44] Table III shows that the interlamellar spacing in the LPBF-D sample is approximately 3 μm , while it is about 7 μm in the SPS sample. In contrast to compressive strength, the wider interlamellar spacing of the SPS-6 sample resulted in a longer creep life. This could lead to diffusion processes in the wider α phase in SPS sample requiring more time compared to in the narrower α phase in the LPBF-D sample, consequently resulting in a longer creep lifetime. This observation suggests that the α/β interface enhances strength during short-time compressive deformation, while the lower volume fraction of the bcc- β phase enhances creep rupture life during long-time deformation.

The longer creep life of the SPS sample compared to any condition of LPBF samples suggests that the homogeneous microstructure in the SPS sample contributes to its superior creep properties.

IV. CONCLUSIONS

In this study, the microstructural characteristics and mechanical properties of Ti-6Al-4Zr-4Nb (wt pct) alloys fabricated by spark plasma sintering (SPS) have been investigated, and the conclusions are as follows:

- (1) Equiaxed α and β phases were formed by sintering at the $\alpha + \beta$ temperature region which was not unlike the bi-modal microstructure obtained in the forged sample. α/β lamellar structures were obtained by sintering at the single β phase region.

The prior β grain sizes of 100 and 200 μm were formed at 90 and 30 MPa, respectively.

- (2) The yield strength depended on grain size and interlamellar spacing during the 200 °C to 600 °C. The yield strength of the SPS sample was lower than that of the LPBF sample but similar to the forged sample.
- (3) The rupture life of the SPS sample was significantly higher than that of the bi-modal forged sample and higher than that of the LPBF-D-HIP sample.
- (4) The creep deformation mechanism is dislocation creep at 550 and 600 °C.

ACKNOWLEDGMENTS

This work was supported by Grants-in Aid for Transformative Research Area A, 21H05198, and The Light Metal Educational Foundation (Japan).

FUNDING

Open Access funding provided by The University of Tokyo.

DATA AVAILABILITY

The raw/processed data required to reproduce these findings cannot be shared at this time as the data also forms part of an ongoing study.

CONFLICT OF INTEREST

The authors declare no conflict of interest associated with this manuscript.

OPEN ACCESS

This article is licensed under a Creative Commons Attribution 4.0 International License, which permits use, sharing, adaptation, distribution and reproduction in any medium or format, as long as you give appropriate credit to the original author(s) and the source, provide a link to the Creative Commons licence, and indicate if changes were made. The images or other third party material in this article are included in the article's Creative Commons licence, unless indicated otherwise in a credit line to the material. If material is not included in the article's Creative Commons licence and your intended use is not permitted by statutory regulation or exceeds the permitted use, you will need to obtain permission directly from the copyright holder. To view a copy of this licence, visit <http://creativecommons.org/licenses/by/4.0/>.

REFERENCES

- International Civil Aviation Organization: *Aviation Benefits Report*, 2019, <https://www.icao.int>. Accessed 25 Sep 2019.
- C. Leyens and M. Peters: *Titanium and Titanium Alloys: Fundamentals and Applications*, Wiley, New York, 2003, pp. 22–25.
- G. Lütjering: *Mater. Sci. Eng. A*, 1998, vol. 243, pp. 32–45.
- H. Mishra, P. Ghosal, T.K. Nandy, and P.K. Sagar: *Mater. Sci. Eng. A*, 2005, vol. 399, pp. 222–31.
- G. Lütjering and J.C. Williams: *Titanium*, Second Edition., 2007, pp. 216–27.
- F.H.S. Froes, M.N. Gungor, and M. Ashraf: *JOM*, 2007, vol. 59, pp. 28–31.
- B. Wysocki, P. Maj, R. Sitek, J. Buhagiar, K. Kurzydłowski, and W. Świąszkowski: *Appl. Sci.*, 2017, vol. 7, p. 657.
- L.E. Murr, S.M. Gaytan, D.A. Ramirez, E. Martinez, J. Hernandez, K.N. Amato, P.W. Shindo, F.R. Medina, and R.B. Wicker: *J. Mater. Sci. Technol.*, 2012, vol. 28, pp. 1–4.
- S. Liu and Y.C. Shin: *Mater. Des.*, 2019, vol. 164, 107552.
- T. Kuroda, H. Masuyama, Y. Toda, T. Matsunaga, T. Ito, M. Watanabe, R. Ozasa, T. Ishimoto, T. Nakano, M. Shimojo, and Y. Yamabe-Mitarai: *Mater. Trans.*, 2023, vol. 64, pp. 95–103.
- Y. Yamabe-Mitarai, T. Inoue, T. Kuroda, S. Matsunaga, Y. Toda, T. Matsunaga, T. Ito, R. Ozasa, T. Ishimoto, and T. Nakano: *Mater. Trans.*, 2023, vol. 64, pp. 1175–82.
- U. Anselmi-Tamburini: in *Encyclopedia of Materials: Technical Ceramics and Glasses*, Elsevier, New York, 2021, pp. 294–310.
- Y.F. Yang and M. Qian: in *Titanium Powder Metallurgy*, Elsevier, New York, 2015, pp. 219–35.
- D. Wimler, J. Lindemann, C. Gammer, P. Spoerk-Erdely, A. Stark, H. Clemens, and S. Mayer: *Mater. Sci. Eng. A*, 2020, vol. 792, 139798.
- O.A. Ogunmefun, B.L. Bayode, T. Jamiru, and Peter.A. Olubambi: *J Alloys Compd.* 2023, vol. 960, p. 170407.
- Y.Q. Zhao, K.Y. Zhu, H.L. Qu, H. Wu, L. Zhou, Y.G. Zhou, W.D. Zeng, and H.Q. Yu: *Mater. Sci. Eng. A*, 2000, vol. 282, pp. 153–57.
- W.F. Cui, C.M. Liu, L. Zhou, and G.Z. Luo: *Mater. Sci. Eng. A*, 2002, vol. 323, pp. 192–97.
- S. Li, T. Deng, Y. Zhang, Y. Liang, R. Li, and T. Dong: *Trans. Indian Inst. Met.*, 2021, vol. 74, pp. 215–22.
- K. Shimagami, T. Ito, Y. Toda, A. Yumoto, and Y. Yamabe-Mitarai: *Mater. Sci. Eng. A*, 2019, vol. 756, pp. 46–53.
- S. Matsunaga, A. Serizawa, and Y. Yamabe-Mitarai: *Mater. Trans.*, 2016, vol. 57, pp. 1902–07.
- R.Z.T.K.S.E.H.M. Y. Yamabe-Mitarai: in *Proc. of the 1st International Conference on 123HiMAT-2015*, 2016, pp. 335–38.
- Y. Yamabe-Mitarai, A. Jastrzebska, T. Kitashima, S. Emura, H. Murakami, R. Zempo, and Z. Pakielka: in *Proceedings of the 13th World Conference on Titanium*, John Wiley & Sons, Inc., Hoboken, NJ, 2016, pp. 917–21.
- K. Shimagami, S. Matsunaga, A. Yumoto, T. Ito, and Y. Yamabe-Mitarai: *Mater. Trans.*, 2017, vol. 58, pp. 1404–10.
- M. Eriksson, Z. Shen, and M. Nygren: *Powder Metall.*, 2005, vol. 48, pp. 231–36.
- C. Menapace, N. Vicente, and A. Molinari: *Powder Metall.*, 2013, vol. 56, pp. 102–10.
- N.S. Weston, F. Derguti, A. Tudball, and M. Jackson: *J. Mater. Sci.*, 2015, vol. 50, pp. 4860–78.
- J. Bustillos, C. Zhang, A. Loganathan, B. Boesl, and A. Agarwal: *Adv. Eng. Mater.*, 2020, vol. 22, p. 2000076.
- M. S. Asl, A. S. Namini, A. Motallebzadeh, and M. Azadbeh: *Mater. Chem. Phys*, 2018, vol. 203, pp. 266–73.
- M. Zadra, F. Casari, L. Girardini, and A. Molinari: *Powder Metall.*, 2008, vol. 51, pp. 59–65.
- T. Borkar and R. Banerjee: *Mater. Sci. Eng. A*, 2014, vol. 618, pp. 176–81.
- M.E. Kassner: *Fundamentals of Creep in Metals and Alloys*, Butterworth-Heinemann, Oxford, 2015, pp. 7–108.
- Z.Y. Ma, R.S. Mishra, and S.C. Tjong: *Acta Mater.*, 2002, vol. 50, pp. 4293–302.
- M. Es-Souni: *Metall. Mater. Trans. A*, 2001, vol. 32A, pp. 285–93.
- M.E. Kassner and M.-T. Pérez-Prado: *Prog. Mater. Sci.*, 2000, vol. 45, pp. 1–2.
- R. Hosseini, M. Morakabati, S.M. Abbasi, and A. Hajari: *Mater. Sci. Eng. A*, 2017, vol. 696, pp. 155–65.
- H. Masuyama, T. Matsunaga, Y. Toda, T. Ito, M. Shimojo, and Y. Yamabe-Mitarai: *Mater. Sci. Forum*, 2021, vol. 1016, pp. 1882–89.
- D.A.P. Reis, C.R.M. Silva, M.C.A. Nono, M.J.R. Barboza, F. Piorino Neto, and E.A.C. Perez: *Mater. Sci. Eng. A*, 2005, vol. 399, pp. 276–80.
- L.A.N.S. Briguente, A.A. Couto, N.M. Guimarães, D.A.P. Reis, C. de Moura Neto, and M.J.R. Barboza: *Defect and Diffusion Forum*, 2012, vol. 326–328, pp. 520–24.
- L. Badea, M. Surand, J. Ruau, and B. Viguier: *Creep behavior of Ti-6Al-4V from 450 °C to 600 °C*, vol. 76, 2014.
- M. Es-Souni: *Mater. Charact*, 2000, vol. 45, pp. 153–64.
- M. Es-Souni: *Mater. Charact*, 2001, vol. 46, pp. 365–79.
- L.M. Viespoli, S. Bressan, T. Itoh, N. Hiyoshi, K.G. Prashanth, and F. Berto: *Eng. Fail. Anal.*, 2020, vol. 111, 104477.
- Y.-K. Kim, S.-H. Park, J.-H. Yu, B. AlMangour, and K.-A. Lee: *Mater. Sci. Eng. A*, 2018, vol. 715, pp. 33–40.
- W. Li, Z. Chen, J. Liu, Q. Wang, and G. Sui: *Mater. Sci. Eng. A*, 2017, vol. 688, pp. 322–29.

Publisher's Note Springer Nature remains neutral with regard to jurisdictional claims in published maps and institutional affiliations.